Frontiers in Bioscience Landmark

Front. Biosci. (Landmark Ed) **2026**; 31(8): 53642
https://doi.org/10.31083/FBL53642

Original Research

CARS1 as a Prognostic Biomarker and Candidate Therapeutic Vulnerability in Hepatocellular Carcinoma: Insights Into Tumor Progression and the Immune Microenvironment

Yezhen Tang[1], Kejun Liu[2], Zhenyao Tan[2], Wei Zhao[1,3,*]

[1]School of Basic Medicine, Ningxia Medical University, 750004 Yinchuan, Ningxia, China
[2]Department of Hepatobiliary Surgery, General Hospital of Ningxia Medical University, 750004 Yinchuan, Ningxia, China
[3]Ningxia Institute of Clinical Medicine, Ningxia People's Hospital, Ningxia Medical University, 750002 Yinchuan, Ningxia, China
*Correspondence: zhaowei@nxmu.edu.cn (Wei Zhao)

Academic Editor: Graham Pawelec
Submitted: 7 May 2026 Revised: 14 July 2026 Accepted: 21 July 2026 Published: 17 August 2026

Abstract

Background: Cysteinyl-tRNA synthetase 1 (CARS1) has been included in ferroptosis-related prognostic signatures, but its clinicopathological relevance, cellular functions, and relationship with the immune microenvironment in hepatocellular carcinoma (HCC) remain incompletely characterized. **Methods:** Transcriptomic and clinical data from The Cancer Genome Atlas Liver Hepatocellular Carcinoma (TCGA-LIHC) dataset were integrated with corresponding data from an institutional HCC tissue cohort of 60 patients. CARS1 expression was evaluated by immunohistochemistry, and immune infiltration was examined using single-sample gene-set enrichment analysis (ssGSEA) and multiplex immunofluorescence, as well as by analyzing public single-cell datasets. The effects of CARS1 depletion were evaluated in MHCC97H and Hep3B cells using Cell Counting Kit-8 (CCK-8) assays, cell-cycle profiling, wound-healing assays, Transwell migration assays, western blotting, and erlotinib-sensitivity assays. **Results:** CARS1 expression was elevated in HCC and was associated with adverse clinicopathological features and poor overall survival. Quantitative immunohistochemistry confirmed elevated CARS1 protein expression in tumor tissues. CARS1 depletion inhibited cell proliferation, altered cell-cycle distribution, impaired migration, and enhanced *in vitro* sensitivity to erlotinib. High CARS1 expression was also associated with increased infiltration of Th2-like immune cells. **Conclusions:** Elevated CARS1 expression is associated with an adverse biological and immune phenotype in HCC. These clinical, histopathological, and loss-of-function findings support further investigation of CARS1 as a prognostic marker and candidate therapeutic target in HCC, although additional mechanistic and *in vivo* validation is required.

Keywords: hepatocellular carcinoma; aminoacyl-tRNA synthetases; prognosis; tumor microenvironment; neoplastic drug resistance

1. Introduction

Hepatocellular carcinoma (HCC) accounts for most primary liver cancers and remains a major cause of cancer mortality worldwide. Global estimates for 2022 indicated approximately 865,000 new liver cancer cases and more than 750,000 deaths [1]. Although resection and transplantation can provide long-term disease control for selected patients, postoperative recurrence remains frequent and continues to compromise overall survival [2,3]. Molecular markers that reflect both tumor behavior and therapeutic susceptibility are therefore needed to improve risk stratification and guide the development of targeted therapies.

The Cysteinyl-tRNA synthetase 1 (*CARS1*) gene encodes the cytosolic enzyme that couples cysteine to its cognate transfer RNA. Beyond this canonical role in translation, CARS1 has been linked to ferroptotic regulation, cellular adaptation to cysteine deprivation, and noncanonical immune signaling through a Toll-like receptor (TLR)2/6-interacting region [4,5,6,7]. More recently, the first CARS1-specific unique structural domain (UNE-C1) was shown to target antigen-presenting cells through TLR2/6 and enhance antigen-specific antitumor immune responses, further supporting the immunological potential of CARS1 [8]. CARS1 has also been incorporated into a ferroptosis- and iron-metabolism-related prognostic signature for HCC [9]. An independent transcriptomic study further associated elevated CARS1 expression with poorer survival, advanced tumor stage, immune-checkpoint expression, and altered immune-cell infiltration in HCC, reinforcing the need for tissue-level and functional validation of CARS1-related phenotypes [10]. These studies establish its potential relevance but do not elucidate whether CARS1 directly contributes to malignant phenotypes in HCC cells or whether its expression marks a distinct immune contexture.

The present study integrated data from the The Cancer Genome Atlas Liver Hepatocellular Carcinoma (TCGA-LIHC), an institutional HCC cohort, and public single-cell datasets, and validated these findings through CARS1 loss-of-function experiments. We examined the association of CARS1 with clinical outcome, assessed its protein expression in human tissues, investigated its relationship with Th2-enriched immune infiltration, and evaluated its effects on cell proliferation, cell-cycle progression, migration, and erlotinib sensitivity. This design aimed to distinguish prog-

nostic associations from experimentally supported cellular functions while avoiding causal interpretations of immune correlations that were not directly tested.

2. Materials and Methods

2.1 Clinical Specimens and Study Design

Formalin-fixed, paraffin-embedded HCC specimens were obtained from 60 patients who underwent surgical treatment at the General Hospital of Ningxia Medical University between January and December 2023. Eligibility criteria included pathological confirmation of HCC, the absence of prior transarterial therapy, chemotherapy, or radiotherapy, and no history of other malignancies. Tumor and adjacent non-tumor liver tissues were collected from the same surgical specimens. Adjacent tissues were histologically confirmed to be free of tumor infiltration. All diagnoses were independently reviewed by two pathologists. Written informed consent was obtained from all participants. The protocol was approved by the Medical Research Ethics Review Committee of the General Hospital of Ningxia Medical University (KYLL-2022-1232), and the research was conducted in accordance with the Declaration of Helsinki.

For clinicopathological analyses, patients were stratified according to the semiquantitative CARS1 immunohistochemical expression score described in Section 2.15. Scores of 1–2 were classified as CARS1-low, whereas scores of 3–4 were classified as CARS1-high. The de-identified clinicopathological data, individual four-tier CARS1 immunohistochemical expression scores, and derived CARS1-low/high categories for the institutional cohort are provided in **Supplementary Table 2**.

2.2 TCGA-LIHC Data Acquisition and Clinical Analyses

Transcriptomic and clinicopathological data for TCGA-LIHC cohort were downloaded from the Genomic Data Commons Data Portal [11]. Representative CARS1 immunohistochemistry images from non-tumor liver and HCC tissues were obtained from the Human Protein Atlas [12]. Cases lacking the variables required for a given analysis were excluded only from that analysis. The expression dataset included 374 tumor samples. CARS1 expression values were log2-transformed, and the median expression value was used to define high- and low-expression groups for survival analyses. Associations with clinical characteristics were evaluated using the available case numbers reported in Table 1. The clinicopathological data for the TCGA-LIHC cases included in each analysis are provided in **Supplementary Table 1**. Overall survival (OS), disease-specific survival (DSS), and progression-free interval (PFI) were analyzed using Kaplan–Meier curves and log-rank tests. Diagnostic discrimination was evaluated by receiver operating characteristic analysis, and associations with OS were assessed using Cox proportional-hazards regression. A separate exploratory nomogram incorporating CARS1 expression and selected clinicopathological variables was constructed to estimate 1-, 3-, and 5-year OS, with calibration curves used for internal assessment.

2.3 Co-Expression, Protein-Interaction, and Enrichment Analyses

Genes co-expressed with CARS1 were identified in the TCGA-LIHC dataset using Pearson correlation, with $|r| > 0.40$ and $p < 0.001$ as the prespecified thresholds. Gene Ontology and Kyoto Encyclopedia of Genes and Genomes enrichment analyses were performed using clusterProfiler [13] (version 4.18.1), and Benjamini–Hochberg-adjusted p values were used to control for multiple testing. A CARS1-centered protein-protein interaction network was generated in the Search Tool for the Retrieval of Interacting Genes/Proteins (STRING) [14] using Homo sapiens as the organism and a minimum interaction score of 0.70. The network was interpreted separately from the transcriptomic co-expression analysis to avoid conflating physical or functional protein associations with mRNA correlation.

2.4 Immune-Infiltration and Single-Cell Analyses

Immune-cell enrichment was estimated in the TCGA-LIHC dataset using single-sample gene-set enrichment analysis (ssGSEA) implemented in the Gene Set Variation Analysis (GSVA) package [15] (version 2.2.0), based on the 24 immune-cell signatures reported by Bindea et al. [16]. Spearman correlation analysis was used to assess the relationships of continuous CARS1 expression with immune-cell enrichment scores, immune-checkpoint genes, and selected Th1- and Th2-associated signatures.

Public T-cell single-cell RNA-sequencing datasets SRS3034951 and SRS3034953 were analyzed in R using Seurat [17] (version 5.2.1). After standard quality control, normalization, variable-feature selection, scaling, principal-component analysis, and graph-based clustering, cell distributions were visualized using t-distributed stochastic neighbor embedding (t-SNE). Cluster-level expression patterns were compared with predefined Th1- and Th2-associated gene sets, and signature scores were summarized for visualization. These analyses were considered exploratory and were not interpreted as evidence that CARS1 directly determines T-cell lineage differentiation.

2.5 In Silico Prediction of Erlotinib Sensitivity

RNA-sequencing expression data for patients with HCC were obtained from the TCGA-LIHC as Fragments Per Kilobase of transcript per Million fragments mapped (FPKM) values and transformed as $\log_2^{(FPKM+1)}$ to generate the expression matrix used for prediction. CARS1 expression was extracted for each tumor sample. Erlotinib sensitivity was predicted using the pRRophetic R package (version 0.5) [18]. The prediction model was trained on the Cancer Genome Project 2016 cell-line dataset, which contains genome-wide gene-expression profiles and exper-

Table 1. Association between CARS1 expression and clinicopathological characteristics in the TCGA-LIHC cohort.

Clinical characteristic	N	Odds ratio	95% CI	*p* value
Sex (male vs female)	374	0.727	0.470–1.122	0.151
Age (>60 vs ≤60 years)	373	1.254	0.835–1.887	0.275
BMI (>25 vs ≤25 kg/m^2)	337	0.675	0.438–1.036	0.073
AFP (>400 vs ≤400 ng/mL)	280	1.164	0.667–2.033	0.592
Albumin (≥3.5 vs <3.5 g/dL)	300	0.998	0.582–1.717	0.993
Prothrombin time (>4 vs ≤4)	297	1.010	0.613–1.660	0.970
Pathological stage (III–IV vs I–II)	350	1.723	1.063–2.821	0.029
T stage (T3–T4 vs T1–T2)	371	1.648	1.027–2.666	0.040
N stage (N1 vs N0)	258	1.048	0.124–8.847	0.963
M stage (M1 vs M0)	272	1.046	0.124–8.819	0.965
Vascular invasion (yes vs no)	318	1.169	0.736–1.859	0.507
Ishak fibrosis score (3–6 vs 0–2)	215	0.758	0.442–1.296	0.312

Odds ratios compare the first category with the second category, which served as the reference. For the Cox regression analysis shown in Fig. 2E, one additional case with missing survival time/event information was excluded; therefore, the available sample sizes in Fig. 2E are one case smaller than those reported in Table 1 for the corresponding variables. AFP, alpha-fetoprotein; BMI, body mass index; CI, confidence interval; CARS1, Cysteinyl-tRNA synthetase 1; TCGA-LIHC, The Cancer Genome Atlas Liver Hepatocellular Carcinoma.

imentally determined half-maximal inhibitory concentration (IC_{50}) values for erlotinib. pRRophetic uses ridge regression to map the tumor-sample expression matrix to estimated erlotinib IC_{50} values, with empirical-Bayes correction applied to reduce systematic differences between the training and tumor datasets. Patients were divided into CARS1-high and CARS1-low groups according to the median CARS1 expression value. Predicted IC_{50} values were compared between the two groups using a two-sided Wilcoxon rank-sum test, and the distributions were visualized with box plots. A p-value < 0.05 was considered statistically significant, and a higher predicted IC_{50} was interpreted as lower predicted sensitivity to erlotinib.

2.6 Cell Culture, Authentication, and CARS1 Silencing

LO2, MHCC97L, MHCC97H, LM3, Hep3B, Huh-7, and SK-HEP-1 cells were obtained from the Cell Bank of the Chinese Academy of Sciences (Shanghai, China). Cells were maintained in Dulbecco's modified Eagle medium (DMEM; catalog no. 12100046; Gibco/Thermo Fisher Scientific, Grand Island, NY, USA) supplemented with 10% fetal bovine serum (FBS; catalog no. FBP-D520; HyCyte/HaiXing Bio, Suzhou, Jiangsu, China), 100 U/mL penicillin, and 100 µg/mL streptomycin at 37 °C in 5% CO2. Small interfering RNAs (siRNAs) targeting CARS1 were synthesized by TsingKe Biological Co., Ltd (Beijing, China). The target sequences were as follows: si-CARS1-1, 5′-AAGCACTCAGCACGGCAGTTG-3′; si-CARS1-2, 5′-AAAGCTGTGCAGTCCAGACTC-3′; and si-CARS1-3, 5′-AACTGGTAGACAGAAACACCT-3′. A non-targeting siRNA served as the negative control. Among the three candidate siRNAs, si-CARS1-3 showed the greatest knockdown efficiency and was therefore used in subsequent functional experiments. Knockdown efficiency was confirmed by quantitative real-time polymerase chain reaction (PCR) and western blotting before functional analysis. The identities of the MHCC97H and Hep3B cell lines used for the functional experiments were confirmed by short tandem repeat profiling performed by an independent commercial service provider. Mycoplasma testing was performed after the cells had been maintained in antibiotic-free medium for more than 48 h and reached approximately 90% confluence, using a one-step loop-mediated isothermal amplification assay (LAMP; catalog no. SNCD-004; Sunncell Biotechnology, Wuhan, Hubei, China). Both cell lines tested negative for mycoplasma contamination. The short tandem repeat (STR) authentication reports and mycoplasma detection report are provided as supplementary files.

2.7 Quantitative Real-Time PCR

Total RNA was isolated from MHCC97H and Hep3B cells using TRIzol reagent (catalog no. 15596026; Thermo Fisher Scientific, Waltham, MA, USA) 48 h after transfection. Following the assessment of RNA concentration and purity, cDNA was synthesized using the PrimeScript™ RT Reagent Kit (Perfect Real Time) (catalog no. RR037A; Takara Bio Inc., Kusatsu, Shiga, Japan). Quantitative PCR was performed using TB Green® Premix Ex Taq™ II (Tli RNaseH Plus) (catalog no. RR820A; Takara Bio Inc., Kusatsu, Shiga, Japan) on a QuantStudio 5 real-time PCR system (Thermo Fisher Scientific, Waltham, MA, USA), with Actin Beta (ACTB) as the internal reference. Relative expression was calculated using the $2^{-\Delta\Delta Ct}$ method.

The primer sequences were as follows: CARS1 forward, 5′-CCACAGAGCCACTTGAGAAA-3′; CARS1 reverse, 5′-AGCCAGTCAGAGAGCAAATC-3′; ACTB forward, 5′-CACTCTTCCAGCCTTCCTTC-3′; and ACTB reverse, 5′-GTACAGGTCTTTGCGGATGT-3′.

2.8 Cell Counting Kit-8 (CCK-8) Assay

Transfected MHCC97H and Hep3B cells were plated in 96-well plates at a density of 3×10^3 cells per well. CCK-8 reagent (catalog no. CA1210; Solarbio Science & Technology, Beijing, China) was added at the indicated time points, and absorbance at 450 nm was measured using a Synergy H1 microplate reader (Agilent Technologies, Santa Clara, CA, USA). Each experiment included technical replicates and was performed independently three times.

2.9 Cell-Cycle Analysis

Transfected cells were harvested following siRNA treatment, washed with phosphate-buffered saline, and fixed in 70% ethanol at 4 °C. Following RNase treatment, cellular DNA was stained using propidium iodide. For the gating strategy, cellular events were first identified on the forward scatter-area/side scatter-area plot to exclude debris and very small particles. Single cells were then selected using forward scatter-area versus forward scatter-height to remove doublets and cell aggregates. The resulting single-cell population was used for propidium iodide-area histogram analysis of DNA content. The proportions of cells in the G0/G1, S, and G2/M phases were quantified using the cell-cycle analysis module in FlowJo software (version 10.10.0; BD Biosciences, Ashland, OR, USA). The same gating strategy was applied consistently to the si-Control and si-CARS1 groups within each cell line. Three independent experiments were analyzed.

2.10 Colony-Formation Assay

MHCC97H and Hep3B cells were seeded into six-well plates at a density of 1000 cells per well after transfection and cultured for 12 days, with the culture medium replaced every 2–3 days. Colonies were then washed with phosphate-buffered saline, fixed with 4% paraformaldehyde, and stained with 0.1% crystal violet. Colonies containing at least 50 cells were counted using ImageJ software (version 1.54p; National Institutes of Health, Bethesda, MD, USA). Colony-formation efficiency was normalized to the corresponding si-Control group. Three independent biological experiments were performed.

2.11 Wound-Healing Assay

MHCC97H cells were plated to form confluent monolayers, and a uniform scratch was created using a sterile pipette tip. Detached cells were removed by washing, and the cultures were maintained in medium containing 3% FBS to minimize proliferation while preserving cell viability and migration. Images were acquired at 0, 24, and 48 h. Wound closure was calculated based on the change in wound area relative to baseline, using the same imaging fields and analysis thresholds for all groups. Three independent experiments were performed.

2.12 Transwell Migration Assay

MHCC97H and Hep3B cell migration was evaluated using uncoated 24-well Transwell inserts with 8-μm pore membranes. After transfection, 5×10^3 viable cells were resuspended in serum-free medium and seeded into the upper chamber, while medium containing 10% FBS was added to the lower chamber as a chemoattractant. After incubation for 24 h, the inserts were carefully removed, and non-migrated cells remaining on the upper surface of the membrane were gently removed with a cotton swab.

The inserts were transferred to new 24-well plates containing 600 μL of 4% paraformaldehyde per well and fixed at room temperature for 30 min. The fixed inserts were then transferred to wells containing approximately 800 μL of 0.1% crystal violet and stained at room temperature for 20 min. After staining, the inserts were gently washed twice with phosphate-buffered saline to remove excess crystal violet.

Migrated cells on the lower surface of the membrane were imaged under a light microscope and counted using ImageJ software. Five randomly selected fields were analyzed for each insert, and the mean cell count from the five fields was used as the value for that insert. Three replicate inserts were analyzed per condition. Individual migrated cells, rather than stained cluster areas, were quantified.

2.13 Erlotinib-Response Assays

Erlotinib (catalog no. HY-50896; MedChemExpress, Monmouth Junction, NJ, USA) was dissolved in dimethyl sulfoxide (DMSO) and diluted in complete culture medium to final concentrations of 0, 1, 2.5, 5, 10, 20, 40, and 80 μM. The 0-μM group received the corresponding vehicle. For the dose-response assays, MHCC97H and Hep3B cells were exposed to erlotinib for 24 h, after which cell viability was measured using the CCK-8 assay and normalized to the vehicle-treated control. Dose-response curves were fitted using a four-parameter nonlinear regression model in GraphPad Prism software (version 8.0; GraphPad Software, San Diego, CA, USA), and the half-maximal inhibitory concentration (IC_{50}) was estimated for each cell line.

For the fixed-dose time-course experiments, transfected cells were assigned to the si-Control, si-Control plus erlotinib, si-CARS1, and si-CARS1 plus erlotinib groups. Erlotinib was applied at a fixed concentration of 10 μM, and cell viability was measured at 12, 24, 48, 72, and 96 h. Each condition was tested in three replicate wells. Time-course data were analyzed using two-way analysis of variance with correction for multiple comparisons. Because formal drug-interaction modeling was not performed, the combined effect was described as enhanced growth inhibition rather than pharmacological synergy.

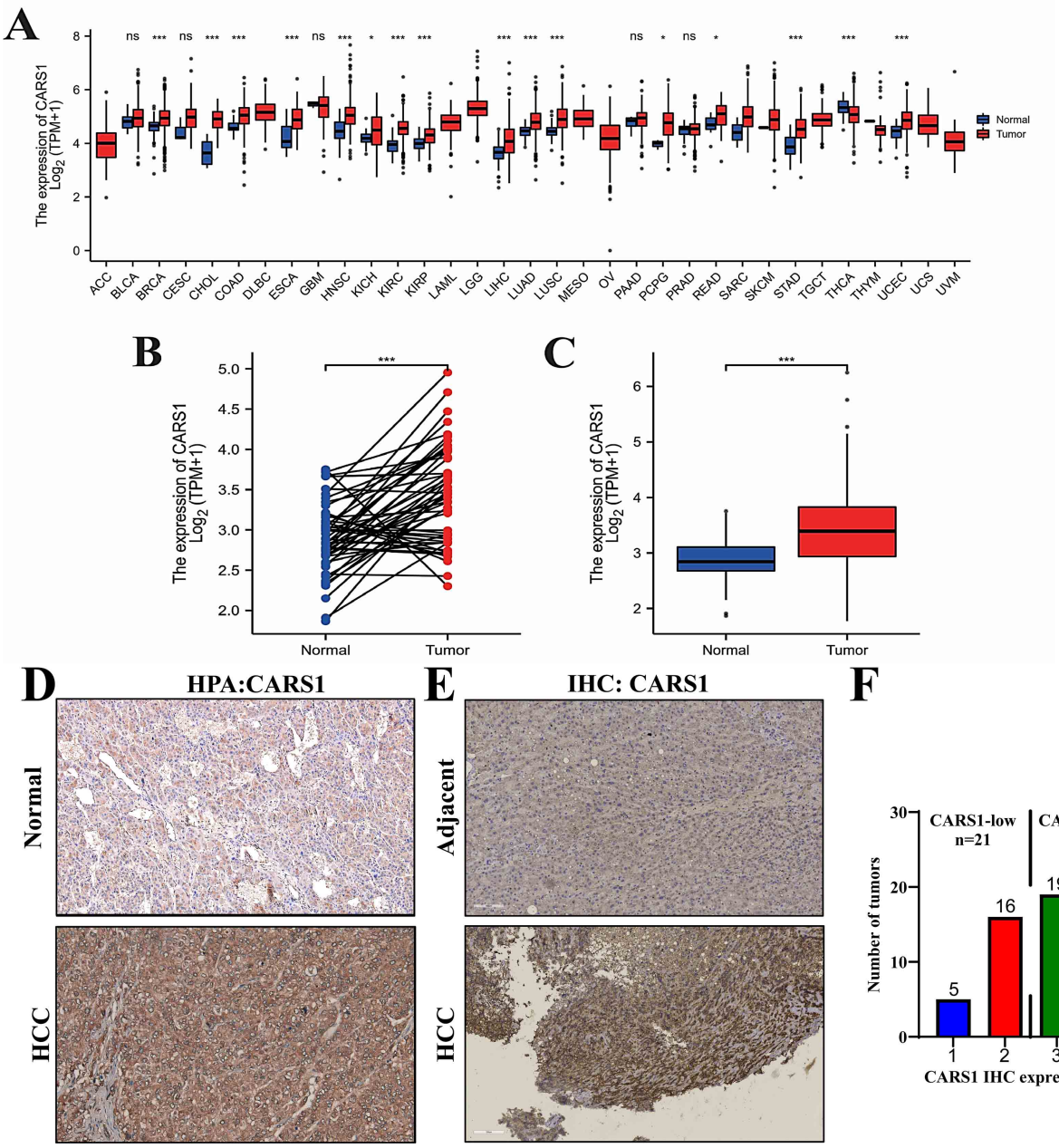

Fig. 1. CARS1 expression in human cancers and HCC tissues. (A) Pan-cancer comparison of CARS1 transcript abundance between tumor and corresponding non-tumor tissues in TCGA. (B) Paired comparison of CARS1 expression in HCC and matched adjacent non-tumor tissues. (C) Unpaired comparison in TCGA-LIHC. (D) Representative CARS1 immunohistochemistry images from the Human Protein Atlas, Scale bars = 100 μm. (E) Representative CARS1 immunohistochemistry images from adjacent non-tumor liver and HCC tissues in the institutional cohort, Scale bars = 100 μm. (F) Distribution of the four-tier CARS1 immunohistochemical expression scores in 60 HCC tumors. Scores of 1–2 were classified as CARS1-low, whereas scores of 3–4 were classified as CARS1-high. Statistical significance is indicated as $^{*}p < 0.05$, $^{***}p < 0.001$; ns, not significant. TPM, Transcripts Per Million; HPA, Human Protein Atlas; IHC, immunohistochemistry; HCC, hepatocellular carcinoma.

2.14 Western Blotting

Cells were lysed in radio-immunoprecipitation assay (RIPA) buffer containing protease and phosphatase inhibitors. Equal amounts of protein were separated by sodium dodecyl sulfate–polyacrylamide gel electrophoresis (SDS-PAGE), transferred to polyvinylidene difluoride membranes, blocked, and incubated overnight at 4 °C with antibodies against CARS1 (1:1000, 15296-1-AP), proliferating cell nuclear antigen (PCNA) (1:1000, 10205-2-AP), matrix metalloproteinase-2 (MMP-2) (1:1000, 66366-1-Ig), or β-actin (1:5000, 81115-1-RR; all from Proteintech), after incubation with the appropriate secondary anti-

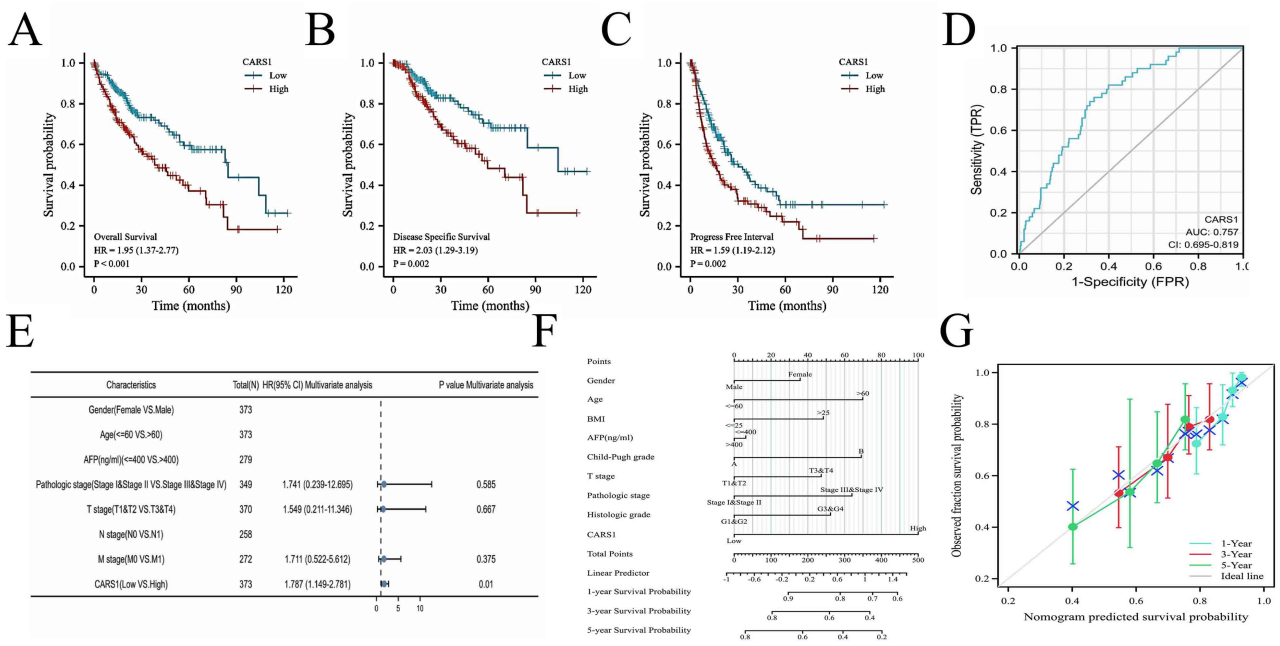

Fig. 2. Clinical and prognostic analyses of CARS1 in TCGA-LIHC. (A–C) Kaplan–Meier curves comparing overall survival, disease-specific survival, and progression-free interval between the CARS1-high and CARS1-low groups. Survival curves were compared using the log-rank test. (D) Receiver operating characteristic curve evaluating the ability of CARS1 expression to distinguish HCC tissues from non-tumor liver tissues; the area under the curve and its 95% confidence interval are shown. (E) Forest plot of the multivariable Cox proportional-hazards model for overall survival. For binary contrasts, the first category is the reference and the hazard ratio represents the second category relative to the first. (F) Exploratory nomogram incorporating CARS1 expression and selected clinicopathological variables to estimate 1-, 3-, and 5-year overall-survival probabilities. (G) Internal calibration curves comparing the nomogram-predicted and observed 1-, 3-, and 5-year overall-survival probabilities. Subgroup overall-survival analyses are presented in **Supplementary Fig. 1**. HR, hazard ratio; AUC, area under the curve; FPR, false positive rate.

Table 2. Univariable and multivariable Cox regression analyses of overall survival in TCGA-LIHC.

Variable	Univariable HR	95% CI	*p* value	Multivariable HR	95% CI	*p* value
Sex (female vs male)	0.793	0.557–1.130	0.200			
Age (≤60 vs >60 years)	1.205	0.850–1.708	0.295			
BMI (≤25 vs >25 kg/m^2)	0.798	0.550–1.158	0.235			
AFP (≤400 vs >400 ng/mL)	1.075	0.658–1.759	0.772			
Ishak fibrosis score (0–2 vs 3–6)	0.740	0.445–1.232	0.247			
Pathological stage (I–II vs III–IV)	2.504	1.727–3.631	<0.001	1.741	0.239–12.695	0.585
T stage (T1–T2 vs T3–T4)	2.598	1.826–3.697	<0.001	1.549	0.211–11.346	0.667
N stage (N0 vs N1)	2.029	0.497–8.281	0.324			
M stage (M0 vs M1)	4.077	1.281–12.973	0.017	1.711	0.522–5.612	0.375
Vascular invasion (no vs yes)	1.344	0.887–2.035	0.163			
CARS1 (low vs high)	1.776	1.251–2.521	0.001	1.787	1.149–2.781	0.010

CI, confidence interval; HR, hazard ratio. For each binary contrast, the first category served as the reference, and the hazard ratio was estimated for the second category relative to the first. Blank cells indicate variables not included in the multivariable model.

bodies. Chemiluminescent signals were visualized using an Amersham Imager 680UV imaging system (Cytiva, Marlborough, MA, USA). Signals were visualized and quantified using ImageJ, with band intensity normalized to β-actin. Molecular weights are indicated on all immunoblot panels.

2.15 Semiquantitative IHC Assessment and Tissue Validation of Th2-Like Infiltration

Four-micrometer-thick formalin-fixed, paraffin-embedded HCC sections were deparaffinized, rehydrated, subjected to heat-induced antigen retrieval in citrate buffer, and treated with 3% hydrogen peroxide. CARS1

Table 3. Association between CARS1 IHC category and clinicopathological variables in the institutional HCC cohort (n = 60).

Characteristic	CARS1-low (n = 21)	CARS1-high (n = 39)	χ^2	*p* value
Age ≤50 years	6 (28.6)	13 (33.3)	0.143	0.705
Age >50 years	15 (71.4)	26 (66.7)		
Female	6 (28.6)	9 (23.1)	0.220	0.639
Male	15 (71.4)	30 (76.9)		
AFP ≤25 ng/mL	10 (47.6)	12 (30.8)	1.669	0.196
AFP >25 ng/mL	11 (52.4)	27 (69.2)		
TBIL ≤22 μmol/L	14 (66.7)	33 (84.6)	2.591	0.107
TBIL >22 μmol/L	7 (33.3)	6 (15.4)		
AST ≤40 U/L	17 (81.0)	19 (48.7)	5.910	0.015
AST >40 U/L	4 (19.0)	20 (51.3)		
ALT ≤40 U/L	14 (66.7)	17 (43.6)	2.911	0.088
ALT >40 U/L	7 (33.3)	22 (56.4)		
ALP ≤135 U/L	18 (85.7)	37 (94.9)	1.499	0.221
ALP >135 U/L	3 (14.3)	2 (5.1)		
Mild cirrhosis	12 (57.1)	26 (66.7)	0.533	0.465
Moderate-severe cirrhosis	9 (42.9)	13 (33.3)		
Tumor size <5 cm	16 (76.2)	16 (41.0)	6.782	0.009
Tumor size ≥5 cm	5 (23.8)	23 (59.0)		
Well differentiated	4 (19.0)	4 (10.3)	0.311	0.577
Moderately/poorly differentiated	17 (81.0)	35 (89.7)		
T1–T2	16 (76.2)	19 (48.7)	4.239	0.040
T3–T4	5 (23.8)	20 (51.3)		
No tumor capsule	14 (66.7)	23 (59.0)	0.342	0.559
Tumor capsule present	7 (33.3)	16 (41.0)		
No satellite nodule	19 (90.5)	28 (71.8)	1.814	0.178
Satellite nodule present	2 (9.5)	11 (28.2)		
No vascular invasion	12 (57.1)	16 (41.0)	1.425	0.233
Vascular invasion present	9 (42.9)	23 (59.0)		
No nerve invasion	20 (95.2)	38 (97.4)	0.000	1.000
Nerve invasion present	1 (4.8)	1 (2.6)		

CARS1 expression was evaluated using a four-tier semiquantitative immunohistochemical expression score. Scores of 1–2 were classified as CARS1-low, whereas scores of 3–4 were classified as CARS1-high, resulting in 21 CARS1-low and 39 CARS1-high tumors. Categorical variables were compared using the chi-square test or Fisher's exact test, as appropriate.

was detected using an anti-CARS1 antibody (1:200; 15296-1-AP, Proteintech, Wuhan, China), visualized using 3,3′-diaminobenzidine, and the sections were counterstained with hematoxylin. Cytoplasmic CARS1 staining in tumor cells was independently assessed by two independent pathologists blinded to the clinicopathological data. Each pathologist assigned a four-tier ordinal expression score from 1 to 4, with higher scores indicating greater CARS1 expression; discrepant assessments were jointly reviewed to reach a consensus final score. Scores of 1–2 were classified as CARS1-low, whereas scores of 3–4 were classified as CARS1-high, yielding 21 CARS1-low and 39 CARS1-high tumors.

Th2-associated immune infiltration was evaluated using tyramide signal amplification-based multiplex immunofluorescence. Following deparaffinization, rehydration, antigen retrieval, endogenous peroxidase blocking, and nonspecific blocking, the sections were sequentially incubated with primary antibodies against cluster of differentiation 4 (CD4), GATA binding protein 3 (GATA3), and CARS1. CD4 was detected using Opal 620 and displayed in red, GATA3 using Opal 570 and displayed in yellow, and CARS1 using Opal 690 and displayed in cyan. Between staining cycles, antibody complexes were removed using heat-mediated antigen retrieval while preserving the deposited fluorophore signals. Nuclei were counterstained with 4',6-Diamidino-2-Phenylindole (DAPI) and displayed in blue.

Whole-slide images were acquired using a Pannoramic MIDI scanner (3DHISTECH Ltd., Budapest, Hungary) under identical settings. Viable tumor regions were manually annotated, whereas necrotic, hemorrhagic, folded, and non-tumor areas were excluded. Positivity for CARS1, CD4, and GATA3 were defined by cyto-

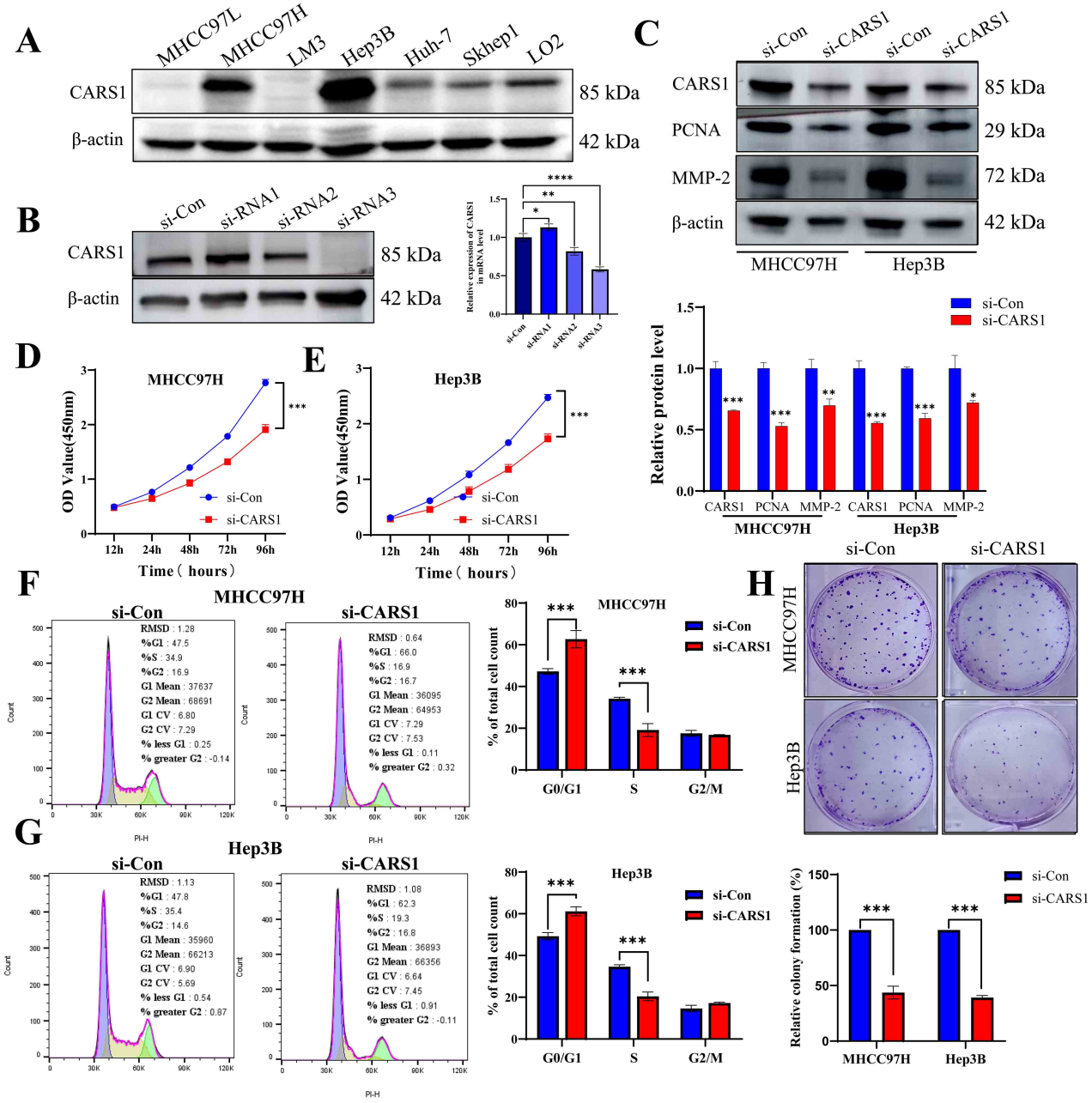

Fig. 3. Effects of CARS1 depletion on HCC cell growth, cell-cycle distribution, and clonogenicity. (A) Basal CARS1 protein expression in liver-derived cell lines. (B) Screening of three CARS1-targeting siRNAs and quantitative assessment of knockdown efficiency. (C) CARS1, PCNA, and MMP-2 protein abundance in MHCC97H and Hep3B cells after CARS1 silencing, with β-actin as the loading control. (D,E) CCK-8 growth curves for MHCC97H and Hep3B cells. (F,G) Representative flow-cytometry distributions and quantification of cells in G0/G1, S, and G2/M phases after CARS1 silencing. (H) Representative colony-formation images and relative colony-formation efficiency in the two cell lines. Data are presented as mean ± standard deviation, and statistical annotations are defined in the figure, $^{*}p < 0.05$; $^{**}p < 0.01$; $^{***}p < 0.001$; $^{****}p < 0.0001$. siRNAs, small interfering RNAs; PCNA, proliferating cell nuclear antigen; MMP-2, matrix metalloproteinase-2; CCK-8, Cell Counting Kit-8.

plasmic, membranous, and nuclear staining, respectively. $CD4^{+}GATA3^{+}$ cells were identified by membranous CD4 and nuclear GATA3 signals within the same segmented cell. Their density was expressed as cells/mm^2, and their proportion among total $CD4^{+}$ cells was also calculated.

$CD4^{+}GATA3^{+}$ cell density and the proportion of $CD4^{+}GATA3^{+}$ cells among total $CD4^{+}$ cells were compared between the CARS1-low and CARS1-high expression groups using the Mann–Whitney U test.

2.16 Statistical Analysis

Statistical analyses were performed using R and GraphPad Prism 8.0 software. Continuous variables were compared using paired or unpaired Student's t tests, Wilcoxon signed-rank tests, or Mann–Whitney U tests, as appropriate. Categorical variables were analyzed using the chi-square test or Fisher's exact test. Longitudinal cell experiments were evaluated by two-way analysis of variance with correction for multiple comparisons. Survival analyses were performed using Kaplan–Meier curves, log-rank tests, and Cox proportional-hazards regression. Spearman correlation analysis was used to assess transcriptomic associations between CARS1 expression and immune-related signatures, whereas multiplex-immunofluorescence measurements were compared between CARS1-low and CARS1-high groups using the Mann–Whitney U test. Data are presented as mean ± standard deviation. All tests were two-sided, and $p < 0.05$ was considered statistically significant.

3. Results

3.1 CARS1 Is Overexpressed in HCC and Validated by Immunohistochemistry in Human Tissues

Pan-cancer analysis showed that CARS1 transcript abundance was increased in multiple malignancies, including liver hepatocellular carcinoma (Fig. 1A). Within the TCGA-LIHC, CARS1 expression was consistently higher in tumor tissue in both paired and unpaired comparisons (Fig. 1B,C). Human Protein Atlas images showed stronger CARS1 staining in HCC than in non-tumor liver tissue (Fig. 1D). In the institutional cohort, CARS1 staining was predominantly localized to the cytoplasm of tumor cells and showed heterogeneous expression across HCC tissues (Fig. 1E). Based on the four-tier immunohistochemical expression score, 5, 16, 19, and 20 tumors received scores of 1, 2, 3, and 4, respectively. Accordingly, 21 tumors were classified as CARS1-low and 39 as CARS1-high (Fig. 1F). Together, the transcriptomic, public protein-expression, and institutional tissue data support frequent CARS1 upregulation in HCC.

3.2 Clinical and Prognostic Significance of CARS1 in HCC

Kaplan–Meier analyses linked high CARS1 expression to shorter OS, DSS, and PFI (Fig. 2A–C), with broadly concordant trends in prespecified clinicopathological subgroups (**Supplementary Fig. 1**). CARS1 showed moderate diagnostic discrimination (Fig. 2D). Multivariable Cox regression showed that high CARS1 expression remained independently associated with shorter OS (hazard ratio [HR] = 1.787, 95% confidence interval [CI]: 1.149–2.781, p = 0.010; Table 2 and Fig. 2E). In the institutional HCC cohort, high CARS1 expression was significantly associated with elevated aspartate aminotransferase levels, larger tumor size, and advanced T stage (Table 3). A separate exploratory nomogram incorporating CARS1 expression and selected clinicopathological variables was developed to estimate 1-, 3-, and 5-year OS, with internal calibration shown in Fig. 2F,G.

3.3 CARS1 Depletion Suppresses HCC Cell Proliferation, Cell-Cycle Progression, and Clonogenicity

CARS1 protein was relatively abundant in MHCC97H and Hep3B cells, which were selected for loss-of-function experiments (Fig. 3A). Screening of three CARS1-targeting siRNAs identified the construct with the strongest suppression, which was used in subsequent assays (Fig. 3B). In both cell lines, CARS1 depletion reduced CARS1, PCNA, and MMP-2 protein abundance (Fig. 3C) and attenuated the increase in CCK-8 signal over time (Fig. 3D,E). Flow-cytometric analysis showed an increased G0/G1 fraction and a reduced S-phase fraction after CARS1 silencing, whereas the G2/M fraction changed comparatively little (Fig. 3F,G). Consistently, CARS1-silenced cells formed fewer colonies than control cells in both MHCC97H and Hep3B cultures (Fig. 3H). These concordant findings indicate that CARS1 supports short-term cell growth, cell-cycle progression, and long-term clonogenic expansion in HCC cells.

3.4 CARS1 Depletion Impairs HCC Cell Motility and Enhances the Growth-Inhibitory Effect of Erlotinib

In MHCC97H monolayers maintained under reduced-serum conditions, CARS1-silenced cells exhibited decreased wound closure than compared with cells at both 24 and 48 h (Fig. 4A). Transwell assays likewise showed fewer migrated cells per field after CARS1 depletion in MHCC97H and Hep3B cells (Fig. 4B,C). These findings, together with the reduction in MMP-2 expression shown in Fig. 3C, support a migration-associated phenotype, although wound closure may still be influenced partly by altered proliferation.

The pRRophetic analysis, based on the median split of TCGA-LIHC tumors, showed that the CARS1-high group had higher predicted erlotinib IC_{50} values than the CARS1-low group, indicating lower predicted drug sensitivity (**Supplementary Fig. 2**). Erlotinib dose-response experiments subsequently established cell-line-specific inhibitory concentrations in MHCC97H and Hep3B cells (Fig. 4D,E). In the fixed-dose experiments, the combination of CARS1 knockdown and erlotinib produced the greatest reduction in cell viability over time in both cell lines (Fig. 4F,G). Because formal drug-interaction modeling was not performed, these findings are interpreted as enhanced erlotinib responsiveness rather than pharmacological synergy.

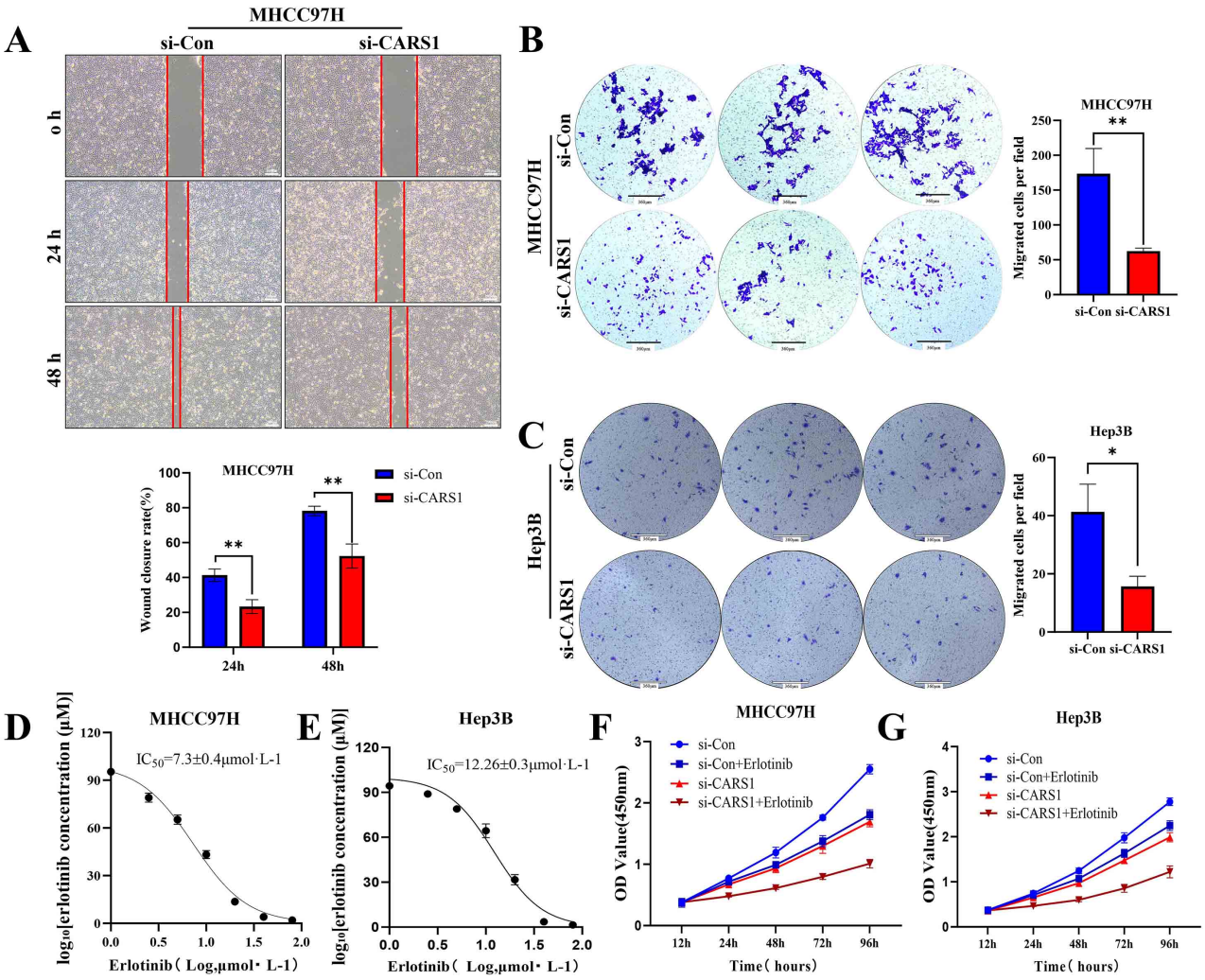

Fig. 4. Effects of CARS1 depletion on HCC cell motility and erlotinib response. (A) Representative wound-healing images of MHCC97H cells at 0, 24, and 48 h and quantitative wound-closure rates. Scale bars = 200 μm. (B,C) Representative Transwell migration fields and numbers of migrated cells per field in MHCC97H and Hep3B cells after CARS1 silencing. Scale bars = 360 μm. (D,E) Erlotinib dose-response curves and estimated IC_{50} values for MHCC97H and Hep3B cells. (F,G) Time-dependent cell viability in si-Control, si-Control plus erlotinib, si-CARS1, and si-CARS1 plus erlotinib groups. Data are presented as mean ± standard deviation. Statistical significance is indicated as $^{*}p < 0.05$ and $^{**}p < 0.01$. IC_{50}, half-maximal inhibitory concentration.

3.5 High CARS1 Expression Is Associated With a Th2-Enriched Immune Contexture

ssGSEA revealed distinct immune-cell enrichment patterns between CARS1-high and CARS1-low TCGA-LIHC tumors. High CARS1 expression was associated with greater enrichment of macrophages, immature dendritic cells, NK CD56bright cells, T-helper cells, follicular helper T cells, and Th2 cells, together with lower pDC and cytotoxic-cell enrichment (Fig. 5A). Detailed Spearman correlation plots for the principal immune-cell signatures are provided in **Supplementary Fig. 3**. CARS1 also showed broad relationships with immune-checkpoint genes (Fig. 5B). In signature-level analyses, continuous CARS1 expression was not meaningfully associated with the selected Th1 signature but was positively associated with the Th2 signature (Fig. 5C,D). Public T-cell single-cell datasets and cluster-level comparisons provided a concordant exploratory pattern favoring Th2-associated marker expression (Fig. 5E–H).

Multiplex immunofluorescence provided tissue-level support for this association. Compared with CARS1-low tumors, CARS1-high tumors contained a higher density of $CD4^{+}GATA3^{+}$ cells and a greater proportion of $CD4^{+}GATA3^{+}$ cells among total $CD4^{+}$ cells (Fig. 5I,J). Together with the transcriptomic association between CARS1 expression and the Th2 signature, these findings support a Th2-enriched immune contexture in CARS1-high HCC tumors but do not establish a continuous tissue-level dose–response relationship or a causal effect of CARS1 on Th2 differentiation.

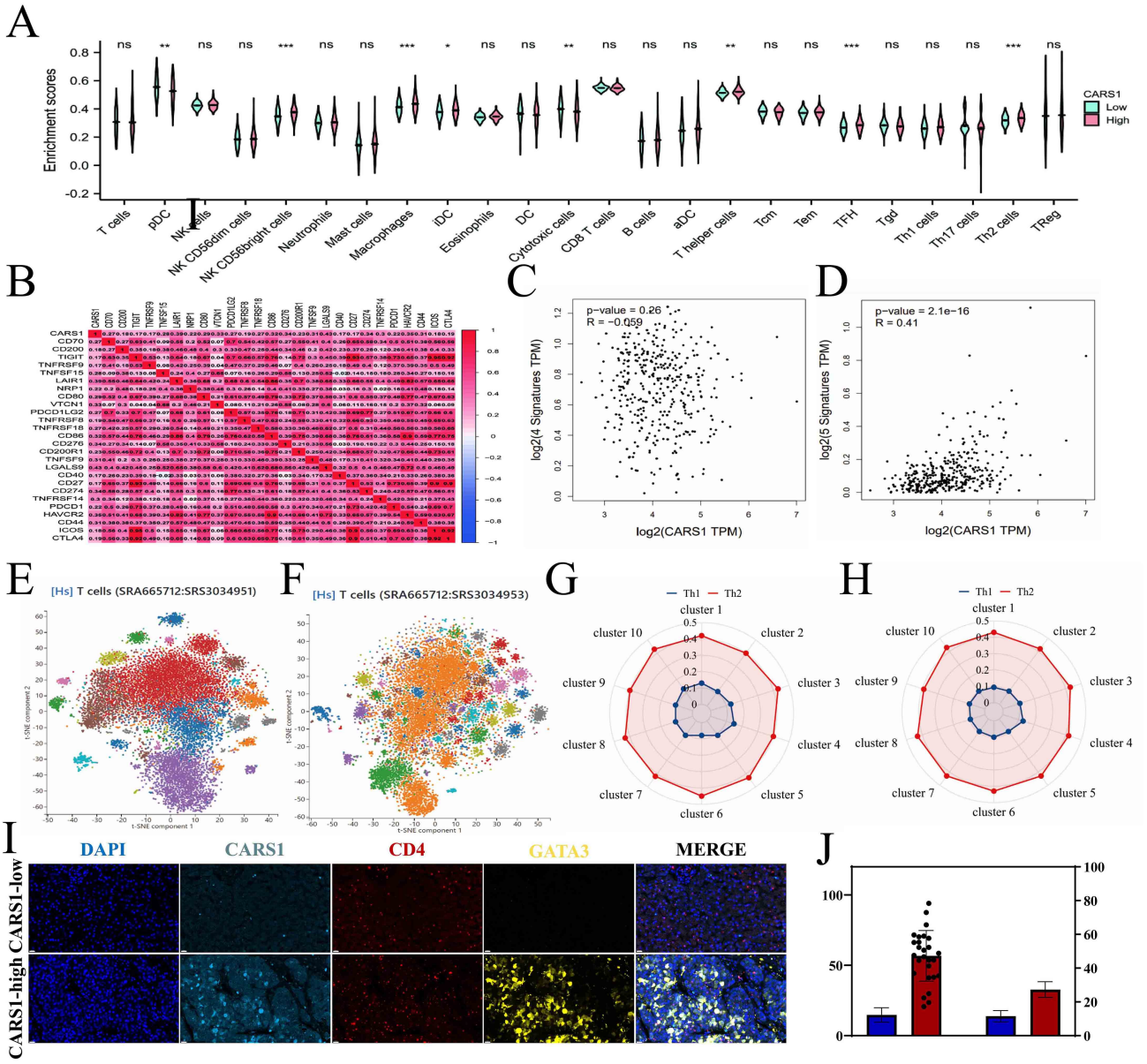

Fig. 5. Association between CARS1 expression and Th2-associated immune features in HCC and public peripheral-blood CD4$^+$ T-cell datasets. (A) ssGSEA enrichment scores for 24 immune-cell signatures in CARS1-high and CARS1-low TCGA-LIHC tumors. (B) Correlation matrix for CARS1 and immune-checkpoint genes. (C,D) Relationships of continuous CARS1 expression with selected Th1- and Th2-associated signatures. (E,F) Single-cell maps of public peripheral-blood CD4$^+$ T-cell datasets SRS3034951 and SRS3034953. (G,H) Cluster-level comparison with Th1- and Th2-associated gene sets in these public CD4$^+$ T-cell datasets. (I) Representative multiplex immunofluorescence images from CARS1-low tumors (IHC scores 1–2) and CARS1-high tumors (IHC scores 3–4); DAPI is shown in blue, CARS1 in cyan, CD4 in red, and GATA3 in yellow (Scale bars = 20 μm). (J) Quantitative comparison of CD4$^+$GATA3$^+$ cell density and the proportion of CD4$^+$GATA3$^+$ cells among total CD4$^+$ cells between CARS1-low (n = 21) and CARS1-high (n = 39) tumors. Group comparisons were performed using the Mann–Whitney U test. Statistical significance is indicated as $^*p < 0.05$, $^{**}p < 0.01$ and $^{***}p < 0.001$; ns, not significant. ssGSEA, single-sample gene-set enrichment analysis; DAPI, 4',6-Diamidino-2-Phenylindole; CD4, cluster of differentiation 4; GATA3, GATA binding protein 3.

3.6 CARS1-Associated Networks Are Enriched in Translation, Ion Transport, and Cell-Adhesion Pathways

The CARS1-centered STRING network contained proteins involved predominantly in aminoacyl-tRNA synthesis and translational processes (Fig. 6A), with detailed functional enrichment of the network shown in **Supplementary Fig. 4**. Transcriptomic co-expression analysis independently identified enrichment in ion transmembrane transport, cell-cell adhesion, ion-channel complexes, neuroactive ligand-receptor interaction, and gap-junction path-

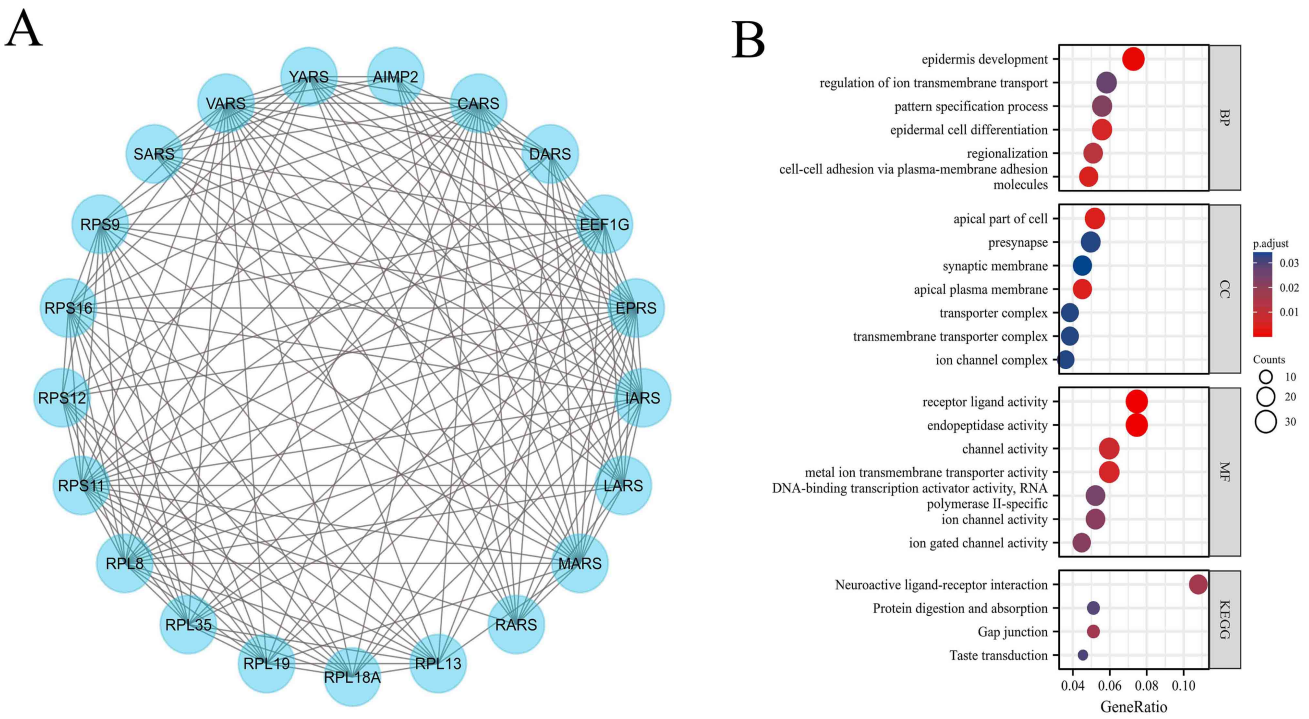

Fig. 6. Protein-interaction and functional-enrichment analyses related to CARS1. (A) CARS1-centered STRING interaction network generated using Homo sapiens and a minimum interaction score of 0.70. (B) Selected Gene Ontology and KEGG terms enriched among CARS1 co-expressed genes; dot size represents gene count and color represents multiple-testing-adjusted significance. STRING, Search Tool for the Retrieval of Interacting Genes/Proteins; KEGG, Kyoto Encyclopedia of Genes and Genomes.

ways (Fig. 6B). Hierarchical functional annotation and representative pathway maps further illustrated ion-transport-related processes, gap-junction signaling, and neuroactive ligand-receptor interactions (**Supplementary Fig. 5**). Because these findings were generated computationally and the candidate pathways were not directly perturbed, they should be regarded as mechanistic hypotheses rather than established downstream pathways of CARS1.

4. Discussion

This study integrated population-level transcriptomic data, a human tissue cohort, and public single-cell datasets, and utilized loss-of-function experiments to characterize the clinical and cellular phenotype associated with CARS1 in HCC. CARS1 was overexpressed in HCC, was associated with adverse clinical features and survival, supported HCC cell proliferation and migration *in vitro*, was associated with a Th2-enriched immune contexture, and influenced the *in vitro* sensitivity to erlotinib.

CARS1 has previously been linked to ferroptosis and cysteine-stress adaptation in several cellular and cancer contexts [4,5,6,7] and has been incorporated into a ferroptosis-related prognostic signature for HCC [9]. The prognostic association alone is therefore not entirely novel. Previous transcriptomic evidence has already linked increased CARS1 expression with unfavorable survival, advanced stage, and altered immune characteristics in HCC [10]. Similarly, recent HCC studies have used integrated transcriptomic screening, immune-infiltration analysis, and cell-based functional validation to identify candidate prognostic biomarkers and experimentally support their roles in tumor progression [19]. The contribution of the present study lies in combining semiquantitative tissue assessment with functional perturbation. Cytoplasmic CARS1 expression was confirmed in the institutional cohort, and high expression was associated with larger tumors, advanced T stage, and elevated aspartate aminotransferase levels. Multivariable survival analysis showed that high CARS1 expression remained independently associated with poorer OS, whereas the diagnostic performance suggested that CARS1 is more likely to contribute to multivariable stratification than to function as a stand-alone diagnostic marker.

The proliferation experiments showed concordant changes in the CCK-8 signal, PCNA abundance, and cell-cycle distribution following CARS1 depletion. The CCK-8 assay reflects both viable cell number and metabolic activity, whereas flow-cytometric cell-cycle analysis helps define the phase-specific basis of the growth phenotype. These assays should therefore be interpreted together rather than as interchangeable measures of proliferation.

Migration-related findings were interpreted cautiously because wound closure is influenced by both lateral movement and proliferation, and prolonged Transwell assays can be affected by cell proliferation after cells reach the lower

membrane. Reduced-serum conditions following scratching, equal viable-cell inputs, consistent observation windows, and individual-cell counting were used to limit these effects. Under these conditions, the persistent reduction in wound closure and Transwell migration supports a motility-related effect. Because a fully documented Matrigel-coated assay was not available, no separate functional invasion claim was made.

The immune analyses linked elevated CARS1 expression to increased Th2-associated enrichment and reduced cytotoxic-cell enrichment in TCGA-LIHC. GATA3 is a canonical regulator of Th2 differentiation [20], and molecularly defined immune subclasses have previously been identified in HCC [21]. Recent spatial proteomic and single-cell studies have further demonstrated that the HCC immune microenvironment is organized into spatially distinct cellular neighborhoods, with clinically relevant differences in immune-cell composition and intercellular interactions [22,23]. These observations support the value of complementing transcriptomic deconvolution with tissue-level multiplex imaging. Multiplex immunofluorescence provided tissue-level support, as CARS1-high tumors exhibited a higher density of $CD4^+GATA3^+$ cells and a greater proportion of double-positive cells among total $CD4^+$ cells than CARS1-low tumors. These findings support an association between CARS1-high HCC and a Th2-enriched immune contexture, but they do not demonstrate a continuous tissue-level correlation or establish directionality. CARS1 may contribute to an immune-permissive tumor state, may be induced by signals that also favor Th2 recruitment, or may serve as a marker for a tumor-cell phenotype that coexists with altered immune composition. Direct evidence that tumor-cell CARS1 drives Th2 polarization would require conditioned-medium or co-culture experiments with primary $CD4^+$ T cells.

CARS1 knockdown enhanced the *in vitro* growth-inhibitory effect of erlotinib. Erlotinib has established activity in selected epidermal growth factor receptor (EGFR)-mutant non-small-cell lung cancers [24], whereas it is not a standard systemic therapy for HCC [3]. Early phase II studies explored erlotinib in advanced HCC [25], but the phase III SEARCH trial did not establish a clinical role for adding erlotinib to sorafenib [26]. EGFR mutational status was not used as a cell-line selection criterion in the present study; the experiments were designed to assess a pharmacological response phenotype rather than to model genotype-selected lung cancer. Dose-response assays established cell-line-specific IC_{50} values, and the fixed-dose experiments showed the greatest suppression of viability when CARS1 depletion was combined with erlotinib. Because formal drug-interaction modeling was not performed, these findings indicate enhanced erlotinib responsiveness rather than pharmacological synergy. Mechanistic studies are required before CARS1 can be proposed as a predictive biomarker for erlotinib in HCC. Recent work on sorafenib resistance in HCC also supports the broader concept that tumor-associated molecular alterations can shape targeted-therapy responsiveness and may provide rational candidates for combination-intervention strategies [27].

The enrichment results suggest links to translation, ion transport, cell adhesion, gap junctions, and neuroactive ligand-receptor signaling. CARS1 itself has experimentally demonstrated noncanonical stress-sensing and immune-signaling functions [6,7], while ion channels can influence tumor proliferation and therapeutic response [28,29]. However, enrichment analyses are sensitive to gene-set composition and do not identify a direct CARS1 substrate or downstream effector. These pathways should therefore be regarded as hypotheses for subsequent mechanistic studies rather than as experimentally confirmed downstream pathways.

5. Limitations

Several limitations should be considered. First, the institutional cohort was obtained from a single center and included 60 patients without an independent tissue validation cohort. Second, the functional experiments relied mainly on transient siRNA-mediated depletion, and rescue experiments would provide stronger evidence against off-target effects. Third, no animal model was included. Fourth, the immune findings were based on computational deconvolution, public single-cell data, and tissue-level associations, which cannot demonstrate that CARS1 directly drives Th2 differentiation or suppresses cytotoxic immunity. Fifth, the erlotinib experiments were conducted *in vitro* and were not designed as a genotype-directed treatment model. Finally, the pathways identified by enrichment analysis were not functionally validated. These limitations constrain the conclusions to biological association and candidate therapeutic vulnerabilities rather than immediate clinical actionability.

6. Conclusion

CARS1 is overexpressed in HCC and is associated with adverse clinicopathological features and poor overall survival. CARS1 depletion suppressed HCC cell proliferation, cell-cycle progression, clonogenicity, and migration while enhancing erlotinib sensitivity *in vitro*. Transcriptomic analyses and categorical tissue comparisons further associated elevated CARS1 expression with a Th2-enriched immune environment. Further rescue, mechanistic, *in vivo*, and external-cohort studies are required before CARS1 can be considered a clinically actionable target.

Availability of Data and Materials

The public datasets analyzed in this study are available from TCGA, the Human Protein Atlas, and the accession numbers stated in the manuscript. Data generated from the institutional cohort and cell experiments are available from the corresponding author upon reasonable request, subject to ethical and privacy restrictions.

Author Contributions

YT: Conceptualization, Methodology, Validation, Investigation, Writing – Original Draft, Writing – Review and Editing, and Visualization. KL: Methodology, Validation, Investigation, Project Administration, and Writing – Review and Editing. ZT: Validation, Formal Analysis, Data Curation, Visualization, and Writing – Review and Editing. WZ: Conceptualization, Resources, Supervision, Funding Acquisition, and Writing – Review and Editing. All authors contributed to editorial revisions of the manuscript. All authors have participated sufficiently in the work, agreed to be accountable for all aspects of the work, read and approved the final manuscript.

Ethics Approval and Consent to Participate

The study was approved by the Ethics Committee of the General Hospital of Ningxia Medical University (approval no. KYLL-2022-1232). Written informed consent was obtained from all participants before sample collection. All procedures involving human participants were performed in accordance with the Declaration of Helsinki.

Acknowledgment

We would like to express our sincere gratitude to all individuals who contributed to this study. We thank the members of our research team for their assistance with experimental procedures, data collection, and manuscript preparation. We also appreciate the constructive comments and suggestions provided by the peer reviewers, which improved the clarity and quality of the manuscript. The Graphical Abstract was created using Figdraw software (https://www.figdraw.com).

Funding

This work was supported by Ningxia Key Research and Development Program (2025BEG01003).

Conflicts of Interest

The authors declare no conflicts of interest.

Supplementary Material

Supplementary material associated with this article can be found, in the online version, at https://doi.org/10.31083/FBL53642.

References

[1] Bray F, Laversanne M, Sung H, Ferlay J, Siegel RL, Soerjomataram I, et al. Global cancer statistics 2022: GLOBOCAN estimates of incidence and mortality worldwide for 36 cancers in 185 countries. CA: a Cancer Journal for Clinicians. 2024; 74: 229–263. https://doi.org/10.3322/caac.21834

[2] Singal AG, Llovet JM, Yarchoan M, Mehta N, Heimbach JK, Dawson LA, et al. AASLD Practice Guidance on prevention, diagnosis, and treatment of hepatocellular carcinoma. Hepatology (Baltimore, Md.). 2023; 78: 1922–1965. https://doi.org/10.1097/HEP.0000000000000466

[3] European Association for the Study of the Liver. EASL Clinical Practice Guidelines on the management of hepatocellular carcinoma. Journal of Hepatology. 2025; 82: 315–374. https://doi.org/10.1016/j.jhep.2024.08.028

[4] Hayano M, Yang WS, Corn CK, Pagano NC, Stockwell BR. Loss of cysteinyl-tRNA synthetase (CARS) induces the transsulfuration pathway and inhibits ferroptosis induced by cystine deprivation. Cell Death and Differentiation. 2016; 23: 270–278. https://doi.org/10.1038/cdd.2015.93

[5] Zhang W, Lin X, Chen S. Cysteinyl-tRNA Synthetase 1 Promotes Ferroptosis-Induced Cell Death via Regulating GPX4 Expression. Journal of Oncology. 2022; 2022: 4849174. https://doi.org/10.1155/2022/4849174

[6] Cho S, Kim SB, Lee Y, Song EC, Kim U, Kim HY, et al. Endogenous TLR2 ligand embedded in the catalytic region of human cysteinyl-tRNA synthetase 1. Journal for Immunotherapy of Cancer. 2020; 8: e000277. https://doi.org/10.1136/jitc-2019-000277

[7] Yuan M, Yan R, Zhang Y, Qiu Y, Jiang Z, Liu H, et al. CARS senses cysteine deprivation to activate AMPK for cell survival. The EMBO Journal. 2021; 40: e108028. https://doi.org/10.15252/embj.2021108028

[8] Kim HY, Cho S, Kim SB, Song EC, Jung W, Shin YG, et al. Specific targeting of cancer vaccines to antigen-presenting cells via an endogenous TLR2/6 ligand derived from cysteinyl-tRNA synthetase 1. Molecular Therapy: the Journal of the American Society of Gene Therapy. 2024; 32: 3597–3617. https://doi.org/10.1016/j.ymthe.2024.07.014

[9] Tang B, Zhu J, Li J, Fan K, Gao Y, Cheng S, et al. The ferroptosis and iron-metabolism signature robustly predicts clinical diagnosis, prognosis and immune microenvironment for hepatocellular carcinoma. Cell Communication and Signaling: CCS. 2020; 18: 174. https://doi.org/10.1186/s12964-020-00663-1

[10] Hu Y, Chen D, Hong M, Liu J, Li Y, Hao J, et al. Apoptosis, Pyroptosis, and Ferroptosis Conspiringly Induce Immunosuppressive Hepatocellular Carcinoma Microenvironment and γδ T-Cell Imbalance. Frontiers in Immunology. 2022; 13: 845974. https://doi.org/10.3389/fimmu.2022.845974

[11] Cancer Genome Atlas Research Network. Comprehensive and Integrative Genomic Characterization of Hepatocellular Carcinoma. Cell. 2017; 169: 1327–1341.e23. https://doi.org/10.1016/j.cell.2017.05.046

[12] Uhlén M, Fagerberg L, Hallström BM, Lindskog C, Oksvold P, Mardinoglu A, et al. Proteomics. Tissue-based map of the human proteome. Science (New York, N.Y.). 2015; 347: 1260419. https://doi.org/10.1126/science.1260419

[13] Wu T, Hu E, Xu S, Chen M, Guo P, Dai Z, et al. clusterProfiler 4.0: A universal enrichment tool for interpreting omics data. Innovation (Cambridge (Mass.)). 2021; 2: 100141. https://doi.org/10.1016/j.xinn.2021.100141

[14] Szklarczyk D, Nastou K, Koutrouli M, Kirsch R, Mehryary F, Hachilif R, et al. The STRING database in 2025: protein networks with directionality of regulation. Nucleic Acids Research. 2025; 53: D730–D737. https://doi.org/10.1093/nar/gkae1113

[15] Hänzelmann S, Castelo R, Guinney J. GSVA: gene set variation analysis for microarray and RNA-seq data. BMC Bioinformatics. 2013; 14: 7. https://doi.org/10.1186/1471-2105-14-7

[16] Bindea G, Mlecnik B, Tosolini M, Kirilovsky A, Waldner M, Obenauf AC, et al. Spatiotemporal dynamics of intratumoral immune cells reveal the immune landscape in human cancer. Immunity. 2013; 39: 782–795. https://doi.org/10.1016/j.immuni.2013.10.003

[17] Hao Y, Hao S, Andersen-Nissen E, Mauck WM, III, Zheng S, Butler A, et al. Integrated analysis of multimodal single-cell data. Cell. 2021; 184: 3573–3587.e29. https://doi.org/10.1016/j.cell.2021.04.048

[18] Geeleher P, Cox N, Huang RS. pRRophetic: an R package for prediction of clinical chemotherapeutic response from tumor gene expression levels. PLoS ONE. 2014; 9: e107468. https://doi.org/10.1371/journal.pone.0107468

[19] Lu X, Chen J, Lu Z, Zang H. Knockdown of *PAK1IP1* can Induce Pyroptosis to inhibit the Progression of Hepatocellular Carcinoma. Frontiers in Bioscience (Landmark Edition). 2025; 30: 26654. https://doi.org/10.31083/FBL26654

[20] Zheng W, Flavell RA. The transcription factor GATA-3 is necessary and sufficient for th2 cytokine gene expression in CD4 t cells. Cell. 1997; 89: 587–596. https://doi.org/10.1016/S0092-8674(00)80240-8

[21] Sia D, Jiao Y, Martinez-Quetglas I, Kuchuk O, Villacorta-Martin C, Castro de Moura M, et al. Identification of an Immune-specific Class of Hepatocellular Carcinoma, Based on Molecular Features. Gastroenterology. 2017; 153: 812–826. https://doi.org/10.1053/j.gastro.2017.06.007

[22] Li M, Wang L, Cong L, Wong CC, Zhang X, Chen H, et al. Spatial proteomics of immune microenvironment in nonalcoholic steatohepatitis-associated hepatocellular carcinoma. Hepatology (Baltimore, Md.). 2024; 79: 560–574. https://doi.org/10.1097/HEP.0000000000000591

[23] Salié H, Wischer L, D'Alessio A, Godbole I, Suo Y, Otto-Mora P, et al. Spatial single-cell profiling and neighbourhood analysis reveal the determinants of immune architecture connected to checkpoint inhibitor therapy outcome in hepatocellular carcinoma. Gut. 2025; 74: 451–466. https://doi.org/10.1136/gutjnl-2024-332837

[24] Zhou C, Wu YL, Chen G, Feng J, Liu XQ, Wang C, et al. Erlotinib versus chemotherapy as first-line treatment for patients with advanced EGFR mutation-positive non-small-cell lung cancer (OPTIMAL, CTONG-0802): a multicentre, open-label, randomised, phase 3 study. The Lancet. Oncology. 2011; 12: 735–742. https://doi.org/10.1016/S1470-2045(11)70184-X

[25] Philip PA, Mahoney MR, Allmer C, Thomas J, Pitot HC, Kim G, et al. Phase II study of Erlotinib (OSI-774) in patients with advanced hepatocellular cancer. Journal of Clinical Oncology: Official Journal of the American Society of Clinical Oncology. 2005; 23: 6657–6663. https://doi.org/10.1200/JCO.2005.14.696

[26] Zhu AX, Rosmorduc O, Evans TRJ, Ross PJ, Santoro A, Carrilho FJ, et al. SEARCH: a phase III, randomized, double-blind, placebo-controlled trial of sorafenib plus erlotinib in patients with advanced hepatocellular carcinoma. Journal of Clinical Oncology: Official Journal of the American Society of Clinical Oncology. 2015; 33: 559–566. https://doi.org/10.1200/JCO.2013.53.7746

[27] Cui L, Liu J, Lv Y, Chen B, Liu K, Bu Y. Study on the Mechanism of CCN2 Promoting Sorafenib Resistance in HCC and Its Combined Intervention Strategy. Frontiers in Bioscience (Landmark Edition). 2025; 30: 45454. https://doi.org/10.31083/FBL45454

[28] Zhao J, Li M, Xu J, Cheng W. The modulation of ion channels in cancer chemo-resistance. Frontiers in Oncology. 2022; 12: 945896. https://doi.org/10.3389/fonc.2022.945896

[29] Wong KK, Banham AH, Yaacob NS, Nur Husna SM. The oncogenic roles of TRPM ion channels in cancer. Journal of Cellular Physiology. 2019; 234: 14556–14573. https://doi.org/10.1002/jcp.28168